

# Modeling the Effect of Atmospheric Gravity Waves on Saturn's Ionosphere

July 12, 2012

Daniel J. Barrow<sup>1</sup>

Katia I. Matcheva<sup>2</sup>

1 Buchholz High School, Gainesville FL 32606

barrowdj@gm.sbac.edu

2 Department of Physics, University of Florida, Gainesville FL 32611-8440

katia@phys.ufl.edu

## Corresponding Author:

Katia I. Matcheva

Department of Physics, University of Florida, P.O. Box 118440, Gainesville FL 32611-8440

e-mail: katia@phys.ufl.edu

phone: (352) 392 0286

## Abstract

Cassini's radio occultations by Saturn reveal a highly variable ionosphere with a complex vertical structure often dominated by several sharp layers of electrons. The cause of these layers has not yet been satisfactorily explained. This paper demonstrates that the observed system of layers in Saturn's lower ionosphere can be explained by the presence of one or more propagating gravity waves. We use a two-dimensional, non-linear, time-dependent model of the interaction of atmospheric gravity waves with ionospheric ions to model the observed periodic structures in two of Cassini's electron density profiles (S08 entry and S68 entry). A single gravity wave is used to reproduce the magnitude, the location, and the shape of the observed peaks in the region dominated by  $H^+$  ions. We also use an analytical model to study small-amplitude variations in the S56 exit electron density profile. We identify three individual wave modes and achieve a good fit to the data. Both models are used to derive the properties (horizontal and vertical wavelengths, period, amplitude, and direction of propagation) of the forcing waves present at the time of the occultations.

**Keywords:** atmospheres, composition; atmospheres, dynamics; ionospheres; Saturn, atmosphere.

# 1 Introduction

Information about the structure of Saturn's ionosphere has increased dramatically since the arrival of the Cassini spacecraft yet our understanding of the underlying processes that maintain its structure has not improved significantly. The bulk of the information comes from radio occultations which return the vertical distribution of electrons. There are 37 electron density profiles available in the literature with 31 of them coming from the Cassini Radio Experiment (Nagy et al., 2006; Kliore et al., 2009). The maximum electron density, the location of the electron density peak as well as the total electron content of the ionosphere show strong variability both with latitude and local time (dusk versus dawn). Despite the observed variability the following trends have been identified: 1) The maximum electron density and the total electron content (TEC) increase with latitude with a maximum in the polar regions and a minimum at the equator (Moore et al., 2010). 2) At low latitudes the dawn electron density peak is smaller than at dusk and occurs at higher altitudes (referred to as dawn/dusk asymmetry) (Nagy et al., 2006; Kliore et al., 2009). 3) A complex system of sharp layers of enhanced electron density is observed in the lower ionosphere at most latitudes. 4) Some profiles exhibit large vertical regions of near depletion of electrons (referred to as bite-outs). Additional information about the structure of the ionosphere at middle latitudes is provided by the detection and the monitoring of Saturn's Electrostatic Discharges (SEDs) which constrain the value of the maximum electron density and show its variation with local time (Fisher et al., 2011).

Modeling of Saturn's ionosphere and fitting of the observed electron density profiles has proven challenging. The pre-Voyager photochemical models overestimated the maximum electron density and predicted the location of the peak to be much lower in the atmosphere than later observed. McElroy (1973) noted that a charge exchange reaction of the dominant  $H^+$  ions with vibrationally excited  $H_2$  molecules decreases the  $H^+$  lifetime. Subsequent models use this mechanism to reduce the predicted electron density peak assuming a range of values for the vibrational temperature of the  $H_2$  molecules. The  $H_2$  vibrational temperature remains unconstrained. Oxygen containing compounds ( $H_2O$  and  $OH$ ) of ring or meteoritic origin are also shown to have an impact on the ionospheric structure (Moses et al., 2000b;

47 Moses and Bass, 2000; Moore et al., 2006). Vertical plasma drifts as a result of neutral  
48 winds or electric fields have been used to move the electron density peak to higher altitudes  
49 (McConnell et al., 1982; Majeed and McConnell, 1991). More recent models employ improved  
50 chemical reaction constants, include realistic modeling of influx of external material ( $H_2O$ ,  
51 metallic ions and dust particles) (Moses and Bass, 2000; Moore and Mendillo, 2007) as well  
52 as take into account the effect of secondary photoelectrons on the ion production rate (Moore  
53 et al., 2010). With the increased number of observations these models face new challenges  
54 as they strive to explain the strong variability seen with latitude and local time.

55 This paper focuses on the effects of atmospheric gravity waves on the ionospheric structure  
56 of Saturn's lower ionosphere. A large fraction of the available electron density profiles show  
57 a system of narrow layers of high electron concentrations. They are present at all latitudes,  
58 both at dawn and dusk conditions, and are usually confined to the region below the main  
59 electron density peak. In a related paper Matcheva and Barrow (2012) analyze all 31 electron  
60 density profiles published to date by the Cassini Radio Science team (Nagy et al. 2006; Kiliore  
61 et al. 2009) for presence of small-scale vertical variability. A wavelet analysis was used to  
62 identify discrete modes of periodicity in the vertical structure of Saturn's ionosphere. The  
63 wavelet analysis alone does not make any assumptions about the nature of the observed  
64 periodicity and the origin of the layers is open for debates. Matcheva and Barrow (2012)  
65 do make a point that the properties of the spectral modes derived from the wavelet analysis  
66 are consistent with atmospheric gravity waves being present in Saturn's upper atmosphere.  
67 Similar systems of multiple layers have been observed in Jupiter's ionosphere (Kliore et  
68 al., 1980; Warwick, et al., 1981; Warwick, 1982; Lindal et al., 1985; Hinson et al. 1997).  
69 Barrow and Matcheva (2011) successfully fit the observed layered structure of the Galileo  
70 J0-ingress electron density with a gravity wave model and demonstrate that atmospheric  
71 gravity waves can easily drive large fluctuations in the ion/electron distribution.

72 Alternative explanations presented in the literature for the origin of the multiple electron  
73 density layers in the lower ionosphere of giant planets include layers of different hydrocarbons  
74 (Kim and Fox, 1994), layers of metallic ions of meteoritic origin (Moses and Bass, 2010; Kim  
75 et al., 2001), and plasma instabilities, but it is yet to be demonstrated how well they can fit  
76 Cassini's observations.

77 This paper has two goals: (1) to demonstrate that atmospheric gravity waves provide  
78 a plausible explanation for the origin of the layers in Saturn’s ionosphere and (2) to derive  
79 the spectral characteristics of the detected wave modes (vertical and horizontal wavelengths,  
80 wave period and amplitude). Ultimately we are interested in studying the impact that  
81 atmospheric gravity waves have on Saturn’s upper atmosphere and to do so we need to  
82 quantify the properties of the waves.

83 The paper uses two different approaches in modeling the effect of atmospheric gravity  
84 waves on the vertical distribution of ions and electrons. In Section 5 we use a fully non-linear  
85 model to simulate the large-amplitude response of Saturn’s ionosphere to traveling gravity  
86 waves and to fit the observed sharp peaks with individual wave modes. In Section 6 we  
87 then use an analytical approach to study small-amplitude variations in the Cassini electron  
88 density profiles. The non-linear simulations provide a realistic treatment of the chemical and  
89 dynamical processes involved, whereas the analytical method allows us to study in detail the  
90 properties of the underlying gravity waves.

## 91 2 Neutral Atmosphere

92 The ionospheric model as well as the wave propagation model used in this work require  
93 knowledge of the vertical structure of the neutral atmosphere. The neutral atmosphere is  
94 modeled as a superposition of a steady state which is a function of altitude only and a small  
95 amplitude perturbation representing a linear gravity wave. Figure 1 presents a summary of  
96 the thermal structure and the chemical composition of the neutral atmosphere in the absence  
97 of atmospheric waves (steady state). Throughout the paper we use the 1 bar pressure level  
98 as a reference altitude.

99 Figure 1

100 The structure of Saturn’s thermosphere has been probed both by Voyager and Cassini  
101 observations using stellar and solar UV occultations (Festou and Atreya 1982, Smith et  
102 al. 1983). Near IR observations of  $H_3^+$  emission from the aurora regions provide information  
103 about the temperature of the atmosphere at high latitudes at the altitude of  $H_3^+$  peak

104 abundance. The available observations show a significant difference in the derived values  
105 for the thermospheric temperature as well as for the location of the homopause (Nagy et  
106 al., 2009). The temperature at 2500 km varies by more than 100 K and the location of the  
107 homopause is quoted to be between 500 and 900 km above the 1 bar pressure level. This  
108 hints either to a real strong variability in Saturn’s upper atmosphere or to a systematic error  
109 in the observations and/or data analysis. In any case this leaves us with a difficult choice for  
110 the thermal structure in the current model for Saturn’s upper atmosphere. The temperature  
111 profile that we use closely resembles the profile suggested by Moses et al. (2000) which is  
112 based on compilations from ground based and space observations (Festou and Atreya 1982;  
113 Smith et al., 1983; Hubbard et al., 1997) as those are the only profiles which are currently  
114 published in peer reviewed journals. At the bottom of the modeled region the atmosphere  
115 is almost isothermal with  $T = 137$  K followed by a fast temperature increase between 800  
116 km and 1300 km and topped by an isothermal layer at  $T = 417$  K. Subsequently we keep in  
117 mind that the temperature in the thermosphere is likely to vary from latitude to latitude as  
118 well as with time.

119 The temperature profile is incorporated in a one dimensional diffusive model to calculate  
120 the vertical distribution of atmospheric species. The location of the hydrocarbon homopause  
121 is determined by the eddy diffusion coefficient and is at about 900 km above the 1 bar pressure  
122 level. The neutral densities are calculated by fixing the mixing ratios for  $He$  and  $CH_4$  at the  
123 bottom boundary of the model ( $z_0=500$  km) and are taken from Conrath and Gautier (2000).  
124 The resulting density profiles for the neutrals are in good agreement with the composition  
125 model from Moses and Bass (2000).

### 126 **3 Atmospheric Gravity Waves**

127 Atmospheric gravity waves are modeled as two dimensional (one vertical and one hori-  
128 zontal) linear small-amplitude perturbations superimposed on the background steady state  
129 of the neutral atmosphere.

130 Atmospheric gravity waves are easily excited in a planetary atmosphere and can prop-  
131 agate over a large distance provided that the atmosphere is stably stratified and that the

132 wave does not get absorbed, reflected, or dissipated along the way. In a non-dissipative atmo-  
133 sphere the wave amplitude grows exponentially with height with a growth rate proportional  
134 to  $\rho^{-1/2}$ , where  $\rho$  is the atmospheric density. As a result a wave generated at the 1 bar  
135 level will have an amplitude that grows about 100 times in magnitude by the time it reaches  
136 Saturn's ionosphere (roughly at 1000 km or  $10^{-4}$  bar). Clearly even a small-amplitude, tro-  
137 pospheric wave would result in a thermospheric wave with a dramatic amplitude which can  
138 easily drive observable signatures in the temperature and the wind structure of the neutral  
139 atmosphere. These fluctuations would inevitably impact the dynamics and the chemistry of  
140 the ionospheric plasma.

141 The atmospheric gravity wave model used in this work is presented in Matcheva and  
142 Barrow (2012) as well as in previous publications (Matcheva and Strobel, 1999; Matcheva  
143 et al., 2000; Barrow and Matcheva, 2011; Barrow et al., 2012). This is a linear, hydrostatic,  
144 quasi-Bussinesque model that allows for slow variations in the background temperature. It  
145 includes the dissipative effect of eddy and molecular viscosity and heat conduction on the  
146 wave motion. The dissipative effect of the ion drag on the neutral wave motion is not included  
147 though it might have a significant effect and would result in dissipation of the waves at lower  
148 altitudes. Molecular dissipation processes become increasingly important with height and  
149 effectively prevent the waves from reaching very high altitudes as they limit the wave growth.

150 In the numerical implementation of the model we use a single linear wave which is im-  
151 posed at the bottom of the simulated region ( $z_0=500$  km) by defining the wave vertical and  
152 horizontal wavenumbers ( $k_z$  and  $k_h$ , respectively), vertical velocity amplitude  $\Delta W(z_0)$  and  
153 phase. We subsequently solve for the temperature, the horizontal, and the vertical veloci-  
154 ties throughout the rest of the region using the corresponding polarization and dispersion  
155 equations (Matcheva and Strobel 1999). The wave field is calculated with a 1 km vertical res-  
156 olution with a time step of 50 s. The horizontal phase is calculated at 20 points along a single  
157 wavelength. The output of the gravity wave model (vertical and horizontal winds) is used  
158 to force the ion motion in both the non-linear simulations and the analytical calculations.

## 159 4 Ionosphere

160 The ionospheric model for Saturn is an adaptation of the Jupiter ionospheric model from  
161 Barrow and Matcheva (2011). This model accounts for the chemistry and dynamics of six  
162 major ion species,  $H^+$ ,  $H_2^+$ ,  $H_3^+$ ,  $He^+$ ,  $HeH^+$ , and  $CH_4^+$  and does a good job at representing  
163 the ionospheric chemistry on Saturn above the homopause (about 900 km) where  $H^+$  and  
164  $H_3^+$  are the dominant ion species. Below the homopause hydrocarbon chemistry dominates  
165 and this model does not represent the chemistry at these altitudes well.

166 Similar to the wave model, the ionospheric model ranges from 500 km to 3000 km in alti-  
167 tude with a vertical step size of 1 km. The horizontal grid is dependent on the wavelength of a  
168 propagating wave; it has 20 grid points along the horizontal direction with periodic boundary  
169 conditions. The model computes the photoproduction of ions due to solar EUV radiation as  
170 well as incorporates secondary electron ionization via the parameterization scheme of Moore  
171 et al. (2009). The ionosphere assumes no steady-state winds. The only winds in the system  
172 are imposed by the propagating gravity waves. The steady state ionosphere is horizontally  
173 homogenous representing the vertical ion distribution in absence of waves at a given latitude  
174 and time of the day. The resulting ionospheric structure is shown in Fig. 2. Above 1100 km  
175 the  $H^+$  ions are dominant whereas below 1100 km the  $H_3^+$  ions dominate the ionosphere.  
176 The calculated background ionosphere is in good agreement with the ionospheric model of  
177 Moses and Bass (2000).

178 Figure 2

179 The lifetime of the main ion constituents is an important factor in determining to what  
180 extent gravity waves can affect the ionospheric structure. If the lifetime of the major ions  
181 is very short then ions and electrons recombine before they can be significantly displaced  
182 from equilibrium. In this instance the perturbations from a gravity wave will be small since  
183 it cannot transport ions a great distance. Conversely, if the lifetime of the major ions is  
184 very long then they are subject to motion along with any large-scale dynamics (Barrow and  
185 Matcheva 2011).

186 Another factor that affects the extent to which a gravity wave can perturb the ionosphere  
187 is the ratio of the ion gyro-frequency to that of the ion-neutral collision frequency. Where the

188 ion gyro-frequency is greater than the ion-neutral collision frequency the ions are constrained  
189 to move along the magnetic field lines. In this case the gravity wave will induce regions of  
190 ion compression and rarefaction. In locations where the ion gyro-frequency is much less than  
191 the ion-neutral collision frequency the ions can move perpendicular to the magnetic field  
192 lines and will not be as efficient in layering the ionosphere. Figure 3 shows the ion gyro-  
193 frequency of  $H^+$ , the  $H^+$  ion-neutral collision frequency, as well as the plasma diffusion time-  
194 scale. The ion gyro-frequency in the ionosphere becomes greater than the collision frequency  
195 at altitudes above 1100 km. The gravity wave-induced perturbations in the electron density  
196 can be significant above this altitude and will be mitigated below this altitude by the neutrals  
197 dragging ions across magnetic field lines.

198 Figure 3

199 Cassini observed Saturn's ionosphere at different latitudes over a couple of seasons and  
200 at different times of the day (dawn/dusk). As a result the ionosphere has been exposed to  
201 a varying magnetospheric flux of incoming charged/neutral particles (not included in the  
202 model) and has been impacted by seasonal changes and different illumination conditions.  
203 Therefore the ionosphere for each observation requires a unique set of model parameters.  
204 Past attempts to explain the observed latitudinal and time variations have included mech-  
205 anisms such as:  $H^+$  quenching via vibrationally excited  $H_2$  (McElroy 1973; Majeed and  
206 McConnell 1996), vertical plasma drifts driven by neutral winds and/or electric fields (Mc-  
207 Connell et al., 1982; Majeed and McConnell, 1991),  $H_2O$  chemistry via influx from Saturn's  
208 rings (Moses and Bass 2000), inclusion of secondary photo electrons and ring-shadowing ef-  
209 fects (Moore et al., 2004, Moore et al. 2010), and electron/ion precipitation. Unfortunately  
210 each of these models depend on unconstrained parameters and so it is unclear to what extent  
211 each mechanism affects the ionosphere. For the purposes of this paper, we make no attempt  
212 to explain the structure of the background ionosphere and its latitudinal and diurnal vari-  
213 ability. Rather, we are interested in showing what effect a wave has on a representative  
214 background ionosphere. To achieve this goal we vary the vibrational temperature of  $H_2$ , in  
215 effect changing the lifetime of  $H^+$  and thus the electron density, in order to produce a repre-  
216 sentative background ionosphere which matches the overall structure of the observed electron

217 density at a given location. It is this ionosphere in which we propagate a gravity wave. The  
218 large number of free parameters certainly allows for an exact match to the background iono-  
219 sphere with the observations though this does not lead to any particular illumination about  
220 what exactly controls the structure of the ionosphere. In this respect we make no attempt to  
221 exactly fit the observation but rather try to capture the main characteristics of the observed  
222 dramatic system of layers in the lower ionosphere.

## 223 5 Ionospheric Response to Large Amplitude Perturba- 224 tions

225 Most of the observed electron density profiles of Saturn's lower ionosphere have a very  
226 complex structure. Matcheva and Barrow (2012) performed a wavelet analysis on 31 Cassini  
227 electron density profiles to study the spectral characteristics of the present scales of vertical  
228 variability. The results revealed a broad range of discrete scales (200-450 km) at most  
229 latitudes with the 300 km scale being most commonly present. A gravity wave model was  
230 used to demonstrate that the characteristics of the detected variability (the location of  
231 the peaks and their relative magnitude) is consistent with the properties of gravity waves  
232 expected to be present in Saturn's upper atmosphere. In this section we use the wave  
233 properties resulting from the wavelet analysis to constrain the vertical wavelength of the  
234 present waves and model their effect on Saturn's ionosphere using our two-dimensional, time-  
235 dependent, non-linear model of the interaction of gravity waves with ionospheric plasma.

236 

Table I
---------

237 The simulations are run for two of Cassini's profiles: S08 entry, a dusk observation at  
238 3°S, and S68 entry, a dusk observation at 28°S (see Table I). The profiles are selected for two  
239 reasons: (1) the vertical scale of variability detected by the wavelet analysis (Figs. 2 and 3 in  
240 Matcheva and Barrow 2012) is consistent with a gravity wave mode and (2) the variability  
241 is dominated by a single vertical scale. Our ionospheric model (Barrow and Matcheva 2011)  
242 allows only for a single propagating wave and could not accurately reproduce the ionosphere  
243 with multiple waves present. It is certainly possible for more than one wave to be present in

244 the ionosphere at the same time. A good example for a multiple wave system detected in a  
245 single observation is the S56 exit observation which we model in Sec. 6.

246 Figures 4 and 5 compare the observed electron density profile (blue dotted line) to the  
247 modeled electron density profile in the presence of atmospheric gravity waves (thick red line).  
248 The waves propagated in the model have the same vertical wavelength as the scales derived  
249 from the wavelet analysis. The parameters of each of the simulated waves are shown in Table  
250 II and the amplitudes are presented in Fig. 6. The results are shown after five wave periods  
251 have elapsed to ensure that any initialization effects had dissipated and that the ionosphere  
252 has reached a quasi-equilibrium state. The initial background electron density profile used  
253 in the model is also shown (thin black line). Note that the initial electron density profile  
254 can be significantly different from the mean profile after the wave has established for a few  
255 periods. This is an expected effect due to a wave driven ion flux along the magnetic field  
256 line (Matcheva et al. 2001).

257 

Figure 4
----------

258 

Figure 5
----------

259 

Figure 6
----------

260 

Table II
----------

261 For both sets the observed electron density and the gravity wave perturbed electron  
262 density profile bear striking similarities. The spacing between peaks, the locations of the  
263 peaks, and the relative amplitude of perturbations are very similar in both cases. The S08  
264 entry data contains three peaks: one at 1700 km, one at 1300 km, and one just below 1000  
265 km. The model recreates the location, spacing, and size of the two higher peaks. It also  
266 demonstrates a remarkable similarity in the overall shape for this profile. The third peak in  
267 the model fails to match the size, location, spacing, and shape of the lowest peak.

268 The S68 entry data contains four peaks: a small peak just below 2000 km, one at 1600 km,  
269 one around 1100 km, and another near 850 km. The model recreates the two upper peaks in  
270 location, spacing, and relative size. The model produces a peak at the same location as the

271 third peak at 1100 km though this peak's shape and amplitude fail to match the observation.  
272 The fourth peak near 850 km is not seen in the simulation. The wavelet analysis of the S68  
273 entry profile shows a significant power at a second, shorter scale (210 km) in the region below  
274 1100 km, which gives rise to the bottom peak at an altitude of 850 km. This explains the  
275 lack of a peak in our simulated results at this altitude.

276 In summary, for both simulations the upper peaks are reproduced well while the modeled  
277 lower peaks are not. This is an expected shortcoming of the model. As described in the pre-  
278 vious section the model does not contain a robust hydrocarbon model and so the chemistry  
279 at these lower heights is not well represented. Further, the ion-neutral collision frequency  
280 becomes comparable to the ion-gyro frequency at around 1100 km so the perturbing mech-  
281 anism itself is not as effective. Both the hydrocarbon chemistry and relative frequencies  
282 reduce the accuracy of the model at the bottom of the ionosphere.

283 Overall, our model of Saturn's ionosphere in the presence of atmospheric gravity waves  
284 recreates the general structure of the observed electron density profiles. These results support  
285 the hypothesis that the observed layers in Saturn's lower ionosphere during the S08 entry  
286 and S68 entry observations are each driven by a single atmospheric gravity wave present at  
287 the time and location of the occultation.

## 288 6 Small Amplitude Simulations

289 The wavelet analysis of the Cassini electron density profiles shows that the present vari-  
290 ability is of diverse scale and magnitude. In addition to the well defined sharp layers that  
291 sometimes dominate the entire vertical profile (for example S08 entry and S68 entry) the  
292 variability in the electron density often has a rather small-amplitude. These small-amplitude  
293 fluctuations can be traced as coherent structures for several scale heights. Because of their  
294 small amplitude these fluctuations can be modeled as linear perturbations superimposed on  
295 the background ionospheric state. Small-amplitude ionospheric fluctuations induced by trav-  
296 eling atmospheric gravity waves can be modeled analytically (Barrow and Matcheva 2011).  
297 The analytical approach provides a better understanding of the forcing waves and the iono-  
298 spheric response avoiding large non-linear effects like wave-induced vertical ion fluxes.

299 The electron density profile obtained during the high latitude S56 exit occultation (71.9°S)  
 300 is a very good example of a profile which has a detectable small-scale periodicity of modest  
 301 amplitude. The detected scales are at  $s_1 = 165$  km,  $s_2 = 250$  km, and  $s_3 = 500$  km each  
 302 peaking at 1200 km, 1000 km, and between 700-1800 km above the 1 bar pressure level  
 303 respectively (Matcheva and Barrow 2012). Figure 7 shows the S56 exit electron density  
 304 profile (left panel) together with the identified scales of variability (right panel). The verti-  
 305 cal structure of the individual scales is obtained by using a wavelet analysis (central panel)  
 306 to decompose the original  $N_e$  profile and to subsequently reconstruct the selected scales  
 307 by using the inverse wavelet transform. A detailed discussion of the wavelet analysis and  
 308 its application to the S56 exit electron density profile is presented in Matcheva and Barrow  
 309 (2012).

310 Figure 7

311 We use our analytical model for wave-driven small-amplitude ion oscillations to fit the  
 312 observations and to extract information about the properties of the forcing waves. In the  
 313 case of a single dominant long-lived ion the resulting electron density perturbation  $N'_e$  is  
 314 described by the following formula (Matcheva et al., 2001; Barrow and Matcheva 2011)

$$N'_e(x, y, z, t) = \frac{N_{e0}(\vec{U}'_n \cdot \hat{l}_b)}{\omega_0} \left[ \vec{k}_r \cdot \hat{l}_b - i \left( \frac{1}{N_{e0}} \frac{\partial N_{e0}}{\partial z} + \frac{1}{2H^*} - k_{zi} \right) (\hat{l}_b \cdot \hat{l}_z) \right]. \quad (1)$$

315 In the equation above  $N_{e0}$  is the background steady state electron density which is a  
 316 function of height only,  $H^*$  is the density scale height, and  $\vec{l}_b$  is a unitw vector in the direction  
 317 of the local magnetic field. The unit vector  $\vec{l}_z$  points up. The forcing wave is given by the  
 318 wave velocity field  $\vec{U}'_n$ , where the subscript  $n$  stands for "neutrals", by the frequency of the  
 319 wave  $\omega_0$ , and by the wave number vector  $\vec{k}$ . The vertical component of the wave number is  
 320 complex and has a real  $k_{zr}$  and an imaginary part  $k_{zi}$ .

321 Equation (1) assumes that the ionosphere is dominated by a single long-lived ion which  
 322 basically means that the ion chemistry is ignored and the electron density is equal to the  
 323 density of the dominant ion. This assumption is well justified for short period waves above  
 324 1100 km where the  $H^+$  ions are thought to dominate. The bottom of the ionosphere is  
 325 complicated by the presence of  $H_3^+$  and  $CH_4^+$  ions and therefore the use of Eq. (1) is not

326 expected to produce reliable results below 1100 km. This region is also complicated by the  
 327 negative values for the electron density derived from the occultation data (Kliore et al. 2009).  
 328 The wavelet analysis and the reconstruction of the small-scale variations is not affected by  
 329 this nor by the exact choice of background  $N_{e0}$  as long as the averaging is done over scales  
 330 longer than 700 km. Figure 7 (left panel) shows two choices of background electron density  
 331 obtained by filtering out scales shorter than 700 km (blue line) and shorter than 2000 km  
 332 (red line) using the inverse wavelet transform. The 700 km line retains the general shape  
 333 of the observed profile better, though it does not avoid the negative values for the electron  
 334 density at the bottom of the ionosphere. For our analytical model we use the profile that  
 335 smoothes out all variations with scales shorter than 2000 km. This ensures positive electron  
 336 density throughout the modeled region.

337 We then proceed with a selection of atmospheric gravity wave parameters to fit the  
 338 identified scales of variability in the data. The vertical wavelength of the waves is already  
 339 determined by the wavelet analysis. The period and the amplitude of the waves, however,  
 340 are not directly constrained by the data. They rely on modeling of the wave propagation  
 341 and dissipation. Figures 8, 9, and 10 show the results from our best fits (left panel) and the  
 342 amplitude profiles of the forcing wave (right panel). The parameters of the gravity waves are  
 343 summarized in Table II. Note that the altitude at which the temperature amplitude of the  
 344 wave is maximum  $z^*$  does not coincide with the location of maximum ionospheric response  
 345  $z_{max}$  (where  $N'_e$  is largest) and hence the discrepancy between the vertical wavelength  $\lambda_z(z^*)$   
 346 and the identified wavelet scale  $s$ . The vertical wavelength varies significantly around 1000  
 347 km because of the large temperature gradient at the homopause.

348 Figure 8

349 Figure 9

350 Figure 10

351 In addition to the vertical and horizontal wavelength the response of the ionosphere  
 352 depends also on the horizontal orientation of the wave with respect to the magnetic field as  
 353 indicated by the  $\vec{k}_r \cdot \hat{l}_b$  term in Eq. (1). In other words the same wave can have very different

354 effect on the ionosphere as it propagates in a North/South or in a East/West direction.  
 355 This dependence can result in an ambiguity in the derived wave parameters but also can be  
 356 exploited to deduce information about the horizontal direction of the wave propagation. To  
 357 illustrate our fitting procedure we will discuss the modeling of the shortest scale  $s_1=165$  km.

358 Figure 11

359 Figure 11 shows the amplitude of the ionospheric response to a 93 km wave with a  
 360 maximum temperature amplitude 23 K. Each panel shows the footprint of the electron  
 361 density perturbation (green shaded area) and the reconstruction of the 165 km scale (red  
 362 solid line). The figure is organized like a table with each row corresponding to a given wave  
 363 period and each column showing results for a given horizontal orientation of the wave number  
 364 vector with respect to the magnetic field. The period is given in the lower left corner and the  
 365 angle is specified in the top right corner of the first column and row respectively. Note that  
 366 23 K is just under the critical amplitude for this vertical wavelength and the results therefore  
 367 show the largest response for a given period and geometric orientation. One can scale the  
 368 amplitude of the response down but cannot increase the predicted ionospheric perturbation  
 369 without exceeding the wave critical amplitude. From the figure it is clear that the ionospheric  
 370 response to short period waves ( $30 < \tau < 60$  min) peaks higher than the observed wavelet  
 371 maximum for  $s_1$ . We also note that the response to these waves does not depend much on  
 372 the angle  $\alpha$ . In contrast, waves with periods longer than 180 min cause the maximum effect  
 373 too low in the ionosphere. We get best fit with a wave that has a period of 120 min. The fit  
 374 to the shape of the reconstructed scale is improved as we vary the angle at which the wave  
 375 propagates. The low right corner of the table is eliminated from the potential options as the  
 376 amplitude of the response is too small. From the shown combinations of wave periods  $\tau$  and  
 377 angles  $\alpha$  the best fit to the observation is  $\tau = 120$  min and  $\alpha = 90^\circ$ . The fit improves a little  
 378 bit for  $\alpha = 108^\circ$  (not shown in this figure). The final fit to the  $s_1$  scale is shown in Fig. 8.

379 For all three scales ( $s, s_2, s_3$ ) we are able to get a reasonable fit to the observed fluctuation  
 380 in amplitude, location of the maximum response, and phase behavior. The quality of the  
 381 fit deteriorates below 1100 km (as expected). The model also does not fit the phase of  
 382 the fluctuations at the top of the ionosphere as our wave model starts violating its original

383 assumptions when the waves are strongly dissipated. The wave corresponding to the  $s1$   
384 scale has the largest amplitude and it is very close to breaking. For the long period waves  
385  $s2$  and  $s3$  the required amplitude is more modest. Both  $s1$  and  $s2$  propagate practically in a  
386 zonal (East-West) direction. We were not able to discriminate strongly between the different  
387 directions of propagation for wave  $s3$ .

388 Figure 12

389 The final comparison between the superposition of all three waves and the S56 exit  
390 observation is shown in Fig. 12. In this figure the individual simulated waves are added to  
391 the background electron density which retains scales longer than 700 km. Clearly the model  
392 captures the main features of the small-scale structure in the observed electron density profile.

## 393 7 Conclusions

394 In this paper we present the results from modeling the ionospheric response of Saturn  
395 to atmospheric gravity waves propagating at high altitudes. The purpose of the project is  
396 twofold: 1) to demonstrate that gravity waves can create layers in the electron distribution  
397 similar to the layers in the Cassini observations and 2) to derive the properties of the waves  
398 present at these heights. We focused our work on three of Cassini's electron density profiles:  
399 S08 entry, S68 entry, and S56 exit which represent low latitude, midlatitude and high latitude  
400 dusk conditions.

401 We use our two-dimensional, non-linear, time-dependent model of the interaction of at-  
402 mospheric gravity waves with ionospheric ions to model the observed periodic structures in  
403 the S08 and S68 observations and our simplified small-amplitude analytical model to study  
404 the S56 observation. The results shown in Figs. 4, 5, and 12 clearly demonstrate that the  
405 gravity wave driven variations provide a good fit to the observations. The vertical parameters  
406 of the forcing waves are constrained by the data and identified by the use of wavelet analysis  
407 (Matcheva and Barrow, 2012). The remaining characteristics of the waves (see Table II) are  
408 derived from our gravity wave propagation/dissipation model and ionospheric interactions.

409 The identified wave modes have relatively modest amplitudes with the 93 km ( $s1=165$   
410 km) scale wave in the S56 exit occultation being close to breaking conditions. The rest of

411 the identified waves have rather long vertical wavelengths and are not expected to break.  
412 All four of the modeled large scale waves have rather long periods ranging from 8 to 9 hours.  
413 Our model did not account for a time dependent solar zenith angle which is needed if more  
414 realistic simulations are desired in the case of vary long period waves. It is interesting to point  
415 that the S08, the S68 and the s2 wave in S56 profiles have very similar characteristics (vertical  
416 wavelength, horizontal wavelength, period and amplitude) although they are propagating at  
417 very different latitudes and result in different effects on the ionosphere.

418 In conclusion we find that gravity waves provide a reasonable explanation for the observed  
419 layered structure of Saturn's lower ionosphere as observed by the Cassini spacecraft.

## 420 References

- 421 1. Barrow, D. and Matcheva, K. I., 2011. Impact of atmospheric gravity waves on the  
422 jovian ionosphere. *Icarus* 211, 609-622.
- 423 2. Barrow, D., Matcheva, K. I., and Drossart, P., 2012. Prospects for Observing At-  
424 mospheric Gravity Waves in Jupiter's Thermosphere Using  $H_3^+$  Emission. *Icarus*, in  
425 press.
- 426 3. Conrath, B. J. and Gautier, D., 2000. Saturn Helium Abundance: A Reanalysis of  
427 Voyager Measurements. *Icarus* 144, Issue *Icarus*, pp. 124-134.
- 428 4. Festou, M. C., and Atreya, S. K., 1982. Voyager ultraviolet stellar occultation mea-  
429 surements of the composition and thermal profiles of the saturnian upper atmosphere.  
430 *Geophys. Res. Lett.* 9, 1147-1150.
- 431 5. Fischer, G. Gurnett, D. A., Zarka, P., Moore, L., Dyudina, U. A., 2011. Peak elec-  
432 tron densities in Saturn's ionosphere derived from the low-frequency cutoff of Saturn  
433 lightning. *Journal of Geophysical Research*, Volume 116, Issue A4.
- 434 6. Gombosi, T. I., Armstrong, T. P., Arridge, C. S., Khurana, K. K., Krimigis, S. M.,  
435 Krupp, N., Persoon, A. M., Thomsen, M. F., 2009. *Saturn from Cassini-Huygens*, by

- 436 Dougherty, Michele K., Esposito, Larry W., Krimigis, Stamatios M., Springer Science  
437 and Business Media B.V., p. 203.
- 438 7. Hubbard, W. B.; Porco, C. C.; Hunten, D. M.; Rieke, G. H.; Rieke, M. J.; McCarthy,  
439 D. W.; Haemmerle, V.; Haller, J.; McLeod, B.; Lebofsky, L. A.; Marcialis, R.; Holberg,  
440 J. B.; Landau, R.; Carrasco, L.; Elias, J.; Buie, M. W.; Dunham, E. W.; Persson, S.  
441 E.; Boroson, T.; West, S.; French, R. G.; Harrington, J.; Elliot, J. L.; Forrest, W.  
442 J.; Pipher, J. L.; Stover, R. J.; Brahic, A.; Grenier, I., 1997. Structure of Saturn's  
443 Mesosphere from the 28 SGR Occultations. *Icarus* 130, 404-425.
- 444 8. Hinson, D. P., Flasar, M. F., Kliore, A. J., Schinder, P. J., Twicken, J. D., Harrera,  
445 R. G., 1997. Results from the first Galileo radio occultation experiment. *J. Geophys.*  
446 *Res. Lett.* 24, 2107-2110.
- 447 9. Kim, Y. H.; Fox, J. L., 1994. The Jovian ionospheric E region. *Geophysical Research*  
448 *Letters*, vol. 18, Feb. 1991, p. 123-126.
- 449 10. Kim, Y. H.; Pesnell, W. Dean; Grebowsky, J. M.; Fox, J. L. 2001. Meteoric Ions in  
450 the Ionosphere of Jupiter. *Icarus*, Volume 150, Issue 2, pp. 261-278.
- 451 11. Kliore, A. J., Nagy, A. F., Marouf, E. A., Anabtawi, A., Barbini, E., Fleischman, D.  
452 U., Kahan, D. S., 2009. Midlatitude and high-latitude electron density profiles in the  
453 ionosphere of Saturn obtained by Cassini radio occultation observations. *Journal of*  
454 *Geophysical Research*, Volume 114, Issue A4, CiteID A04315.
- 455 12. Kliore, A. J.; Patel, I. R.; Lindal, G. F.; Sweetnam, D. N.; Hotz, H. B.; Waite, J.  
456 H.; McDonough, T. 1980. Structure of the ionosphere and atmosphere of Saturn from  
457 Pioneer 11 Saturn radio occultation. *Journal of Geophysical Research*, vol. 85, Nov.  
458 1, 1980, p. 5857-5870.
- 459 13. Lindal, G. F., Sweetnam, D. N., and Eshleman, V. R., 1985. The atmosphere of Saturn:  
460 An analysis of the Voyager radio occultation measurements. *Astron. J.* 90, 1136-1146.
- 461 14. Majeed, T., McConneall, J. C., 1991. The upper ionospheres of Jupiter and Saturn.  
462 *Planetary and Space Science*, vol. 39, 1715-1732.

- 463 15. Majeed, T., McConneell, J. C., 1996. Voyager electron density measurements on Sat-  
464 urn: Analysis with a time dependent ionospheric model. *Journal of Geophysical Re-*  
465 *search*, Volume 101, Issue E3, 7589-7598.
- 466 16. Matcheva, K., Barrow, D., 2012. Small-Scale Variability in Saturn's Lower Ionosphere.  
467 Submitted to *Icarus* 2012.
- 468 17. Matcheva, K. I., and Strobel D. F., 1999. Heating of Jupiter's thermosphere by dis-  
469 sipation of gravity waves due to molecular viscosity and heat conduction. *Icarus* 140,  
470 328-340.
- 471 18. Matcheva, K. I., Strobel, D. F., Flasar, F. M., 2001. Interaction of gravity waves with  
472 ionospheric plasma: Implications for Jupiter's ionosphere. *Icarus* 152, 347-365.
- 473 19. McElroy, M., 1973. The Ionospheres of the Major Planets. *Space Science Reviews* 14,  
474 Issue 3-4, 460-473.
- 475 20. Moore, L. E., Mendillo, M., Mueller-Wodarg, I. C. F., Murr, D. L., 2004. Modeling of  
476 global variations and ring shadowing in Saturn's ionosphere. *Icarus* 172, 503-520.
- 477 21. Moore, L., Nagy, A., Kliore, A., Mueller-Wodarg, I., Richardson, J., Mendillo, M. 2006.  
478 Cassini radio occultations of Saturn's ionosphere: Model comparisons using a constant  
479 water flux. *Geophysical Research Letters*, vol. 33, L22202.
- 480 22. Moore, L., and Mendillo, M., 2007. Are plasma depletions in Saturn's ionosphere a  
481 signature of timedependent water input? *Geophysical Research Letters*, 34, L12202.
- 482 23. Moore, L.; Galand, M.; Mueller-Wodarg, I.; Mendillo, M., 2009. Response of Saturn's  
483 ionosphere to solar radiation: Testing parameterizations for thermal electron heating  
484 and secondary ionization processes. *Planetary and Space Science*, Volume 57, Issue  
485 14-15, 1699-1705.
- 486 24. Moore, L., Mueller-Wodarg, I., Galand, M., Kliore, A., Mendillo, M., 2010. Latitudi-  
487 nal variations in Saturn's ionosphere: Cassini measurements and model comparisons.  
488 *Journal of Geophysical Research*, Volume 115, Issue A11, CiteID A11317.

- 489 25. Moses, J. I. and Bass, S. F., 2000. The effects of external material on the chemistry  
490 and structure of Saturn's ionosphere. *Journal of Geophysical Research*, Volume 105,  
491 Issue E3, 7013-7052.
- 492 26. Moses, J. I., Bezard, B., Lellouch, E., Gladstone, G., Feuchtgruber, H., Allen, M., 2000,  
493 Photochemistry of Saturn's Atmosphere: I. Hydrocarbon Chemistry and Comparison  
494 with ISO Observations. *Icarus* 143, 244-298.
- 495 27. Moses, J. I., Bezard, B., Lellouch, E., Gladstone, G., Feuchtgruber, H., Allen, M.,  
496 2000b. Photochemistry of Saturn's Atmosphere II. Effects of an Influx of External  
497 Oxygen. *Icarus* 145, 166-202.
- 498 28. Nagy, A. F., Kliore, A. J., Marouf, E., French, R., Flasar, M., Rappaport, N. J.,  
499 Anabtawi, A., Asmar, S. W., Johnston, D., Barbini, E., Goltz, G., Fleischman, D.,  
500 2006. First results from the ionospheric radio occultations of Saturn by the Cassini  
501 spacecraft. *Journal of Geophysical Research*, Volume 111, Issue A6, CiteID A06310.
- 502 29. Nagy, A. , Arvydas J. Kliore, Michael Mendillo, Steve Miller, Luke Moore, Julianne  
503 I. Moses, Ingo Mueller-Wodarg, and Don Shemansky, 2009. Upper Atmosphere and  
504 Ionosphere of Saturn. in "Saturn from Cassini-Huygens", by Dougherty, Michele K.;  
505 Esposito, Larry W.; Krimigis, Stamatios M., ISBN 978-1-4020-9216-9. Springer Science  
506 Business Media B.V., p. 181.
- 507 30. Smith, G. R., Shemansky, D. E., Holberg, J. B., Broadfoot, A. L., Sandel, B. R., and  
508 McConnell, J. C., 1983. Saturn's upper atmosphere from the Voyager 2 EUV solar and  
509 stellar occultations. *J. Geophys. Res.* 88, 8667-8678.
- 510 31. Warwick, J. W., Evans, D. R., Romig, J. H., Alexander, J. K., Desch, M. D., Kaiser,  
511 M. L., Aubier, M. G., Leblanc, Y., Lecacheux, A., Pedersen, B. M., 1982. Planetary  
512 radio astronomy observations from Voyager 2 near Saturn. *Science*, vol. 215, Jan. 29,  
513 1982, p. 582-587.
- 514 32. Warwick, J. W., Pearce, J. B., Evans, D. R., Carr, T. D., Schauble, J. J., Alexander,  
515 J. K., Kaiser, M. L., Desch, M. D., Pedersen, M., Lecacheux, A., Daigne, G., Boisshot,

516 A., Barrow, C. H., 1981. Planetary radio astronomy observations from Voyager 1 near  
517 Saturn. *Science*, vol. 212, Apr. 10, 1981, p. 239-243.

518 **List of Tables:**

519

520 **Table I:** Observation parameters for the Cassini radio occultations used in this paper (Nagy  
521 et al., 2006; Kliore et al., 2009). The magnetic field inclination is based on the Gombosi et  
522 al. (2009) model of Saturn’s magnetic field.

523 **Table II:** Parameters of the gravity waves used in the large and small amplitude simulations  
524 in Sections 5 and 6. The vertical wavelength  $\lambda_z$  and the wave temperature amplitude  $T_{max}$   
525 are quoted at the altitude of wave maximum amplitude  $z^*$ . The scale  $s$  is given at the  
526 altitude of maximum wavelet coefficient  $z_{max}$ .  $\alpha$  is the angle between the direction of the  
527 wave number vector and the magnetic field in the horizontal plane.

TABLE I

Observation	Latitude	Dawn/Dusk	SZA	$\vec{B}$ inclination
S08 entry	3.1°S	dusk	85.2°	12°
S68 entry	27.7°S	dusk	83.8°	43°
S56 exit	71.7°S	dusk	89.6°	77°

Table I: Observation parameters for the Cassini radio occultations used in this paper (Nagy et al., 2006; Kliore et al., 2009). The magnetic field inclination is based on the Gombosi et al. (2009) model of Saturn’s magnetic field.

TABLE II

Occultation	$s$	$z_{max}$	$z^*$ [km]	$\lambda_z(z^*)$ [km]	$\lambda_h$ [km]	$\tau$ [min]	$T_{max}(z^*)$ [K]	$\alpha$ [deg.]
S08 entry	380	1250	1102	244	7000	470	8	0
S68 entry	430	1350	1102	244	7000	470	4	0
S56 exit	165	1200	1050	93	791	120	23	108
	250	1000	1090	225	7792	550	12.5	120
	500	1500	1526	652	11987	573	2.2	0

Table II: Parameters of the gravity waves used in the large and small amplitude simulations in Sections 5 and 6. The vertical wavelength  $\lambda_z$  and the wave temperature amplitude  $T_{max}$  are quoted at the altitude of wave maximum amplitude  $z^*$ . The scale  $s$  is given at the altitude of maximum wavelet coefficient  $z_{max}$ .  $\alpha$  is the angle between the direction of the wave number vector and the magnetic field in the horizontal plane.

530 List of Figures and figure captions:

531

532 **Figure 1:** Steady state neutral atmosphere: composition (bottom axis) and temperature  
533 (top axis) profiles.

534

535 **Figure 2:** Steady state ionospheric model: vertical ion distribution for average midlati-  
536 tude conditions.

537

538 **Figure 3:** Relevant dynamical time (frequency) constants:  $H^+$  gyro frequency (black  
539 solid line);  $H^+$  collisional frequency (black dashed line);  $1/t_d$ , where  $t_d$  is the  $H^+$  diffusion  
540 time constant (black dotted line); buoyancy frequency of the atmosphere (gray dotted line);  
541  $1/t_S$ , where  $t_S$  is the length of one Saturn day (gray solid line).

542

543 **Figure 4:** Large amplitude simulation for the S08 entry occultation. Dotted line - ob-  
544 served electron density; thin black line - initial steady state electron density (no waves);  
545 thick solid red line - wave-perturbed electron density after five wave periods.

546

547 **Figure 5:** Same as Fig. 4 but for S68 entry.

548

549 **Figure 6:** Vertical amplitude profiles of the temperature  $T$ , the horizontal velocity  $V$ ,  
550 and the vertical velocity  $W$  of the forcing waves in the case of S08 entry occultation (left  
551 panel) and the S68 entry occultation (right panel).

552

553 **Figure 7:** S56 exit radio occultation. Left panel: observed electron density profile (black  
554 line); wavelet reconstruction for scales longer than 700 km (blue line); wavelet reconstruction  
555 for scales longer than 2000 km (red line). Central panel: Wavelet decomposition map for  
556 the S56 exit observation. The amplitude of the vertical variations in the observed  $N_e$  profile  
557 is shown as a function of scale and altitude. Contours (solid black lines) are drawn at 5%  
558 increments. Right panel: Reconstruction of the detected scales  $s_1 = 165$  km,  $s_2 = 250$  km,  
559  $s_3 = 500$  km. The reconstructed scales are shifted on the horizontal axis for clarity.

560

561 **Figure 8:** Best fit for scale 1. Left panel: Wavelet reconstruction for scale 1 ( $s1 = 165$   
562 km) (black line) and the best fit to the data (green line) based on our analytical small-  
563 amplitude model of a gravity wave interaction with the ionosphere. Right panel: Vertical  
564 amplitude profiles of the temperature  $T$ , horizontal velocity  $V$ , and vertical velocity  $W$  of  
565 the forcing wave. The critical temperature  $T_{cr}$  is shown as a blue line. Note that this wave  
566 is close to breaking conditions.

567

568 **Figure 9:** Same as in Fig. 8 but for scale 2 ( $s2 = 250$  km)

569

570 **Figure 10:** Same as in Fig. 8 but for scale 3 ( $s3 = 500$  km).

571

572 **Figure 11:** Response table for scale 1. The modeling is done for a wave with  $\lambda_z(z_{max}) =$   
573 165 km ( $\lambda_z(z^*) = 93$  km). The period of the wave is shown in the bottom left corner and  
574 the angle of propagation  $\alpha$  is given in the top right corner of the most left and top panels.  
575 Panels in the same row show a wave with the same period and panels in a given column  
576 have the same angle  $\alpha$ . Each panel shows the amplitude of the resulting electron density  
577 perturbations (the contour of the green shaded area) and the  $s1$  scale (red line), plotted  
578 once with a positive and once with a negative sign). From the shown cases the closest fit is  
579 achieved for  $\tau = 120$  min and  $\alpha = 90^\circ$ . Our best fit is for  $\tau = 120$  min and  $\alpha = 108^\circ$ (not  
580 shown here).

581

582 **Figure 12:** Comparison between S56 exit observation (black line) and the small-  
583 amplitude simulation model (red line). The ionospheric results from the three waves are  
584 added together and superimposed on the background electron density profile shown in Fig. 7.

585

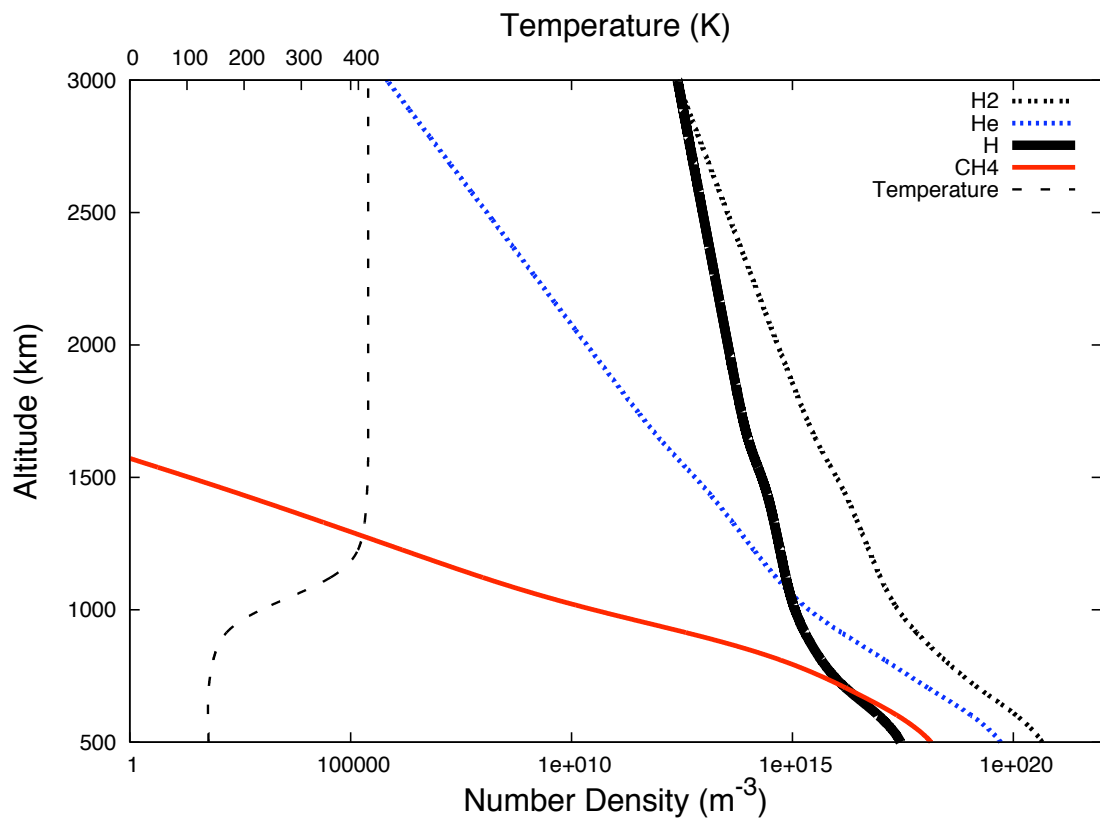


Figure 1: Steady state neutral atmosphere: composition (bottom axis) and temperature (top axis) profiles.

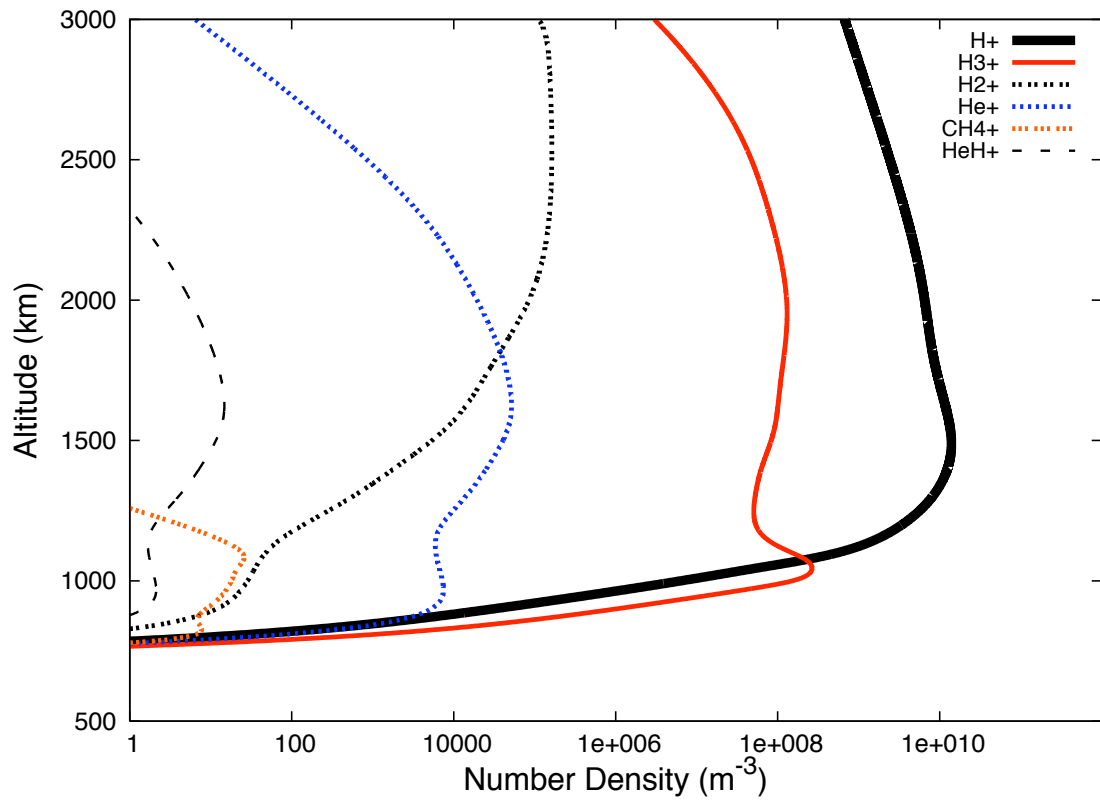


Figure 2: Steady state ionospheric model: vertical ion distribution for average midlatitude conditions.

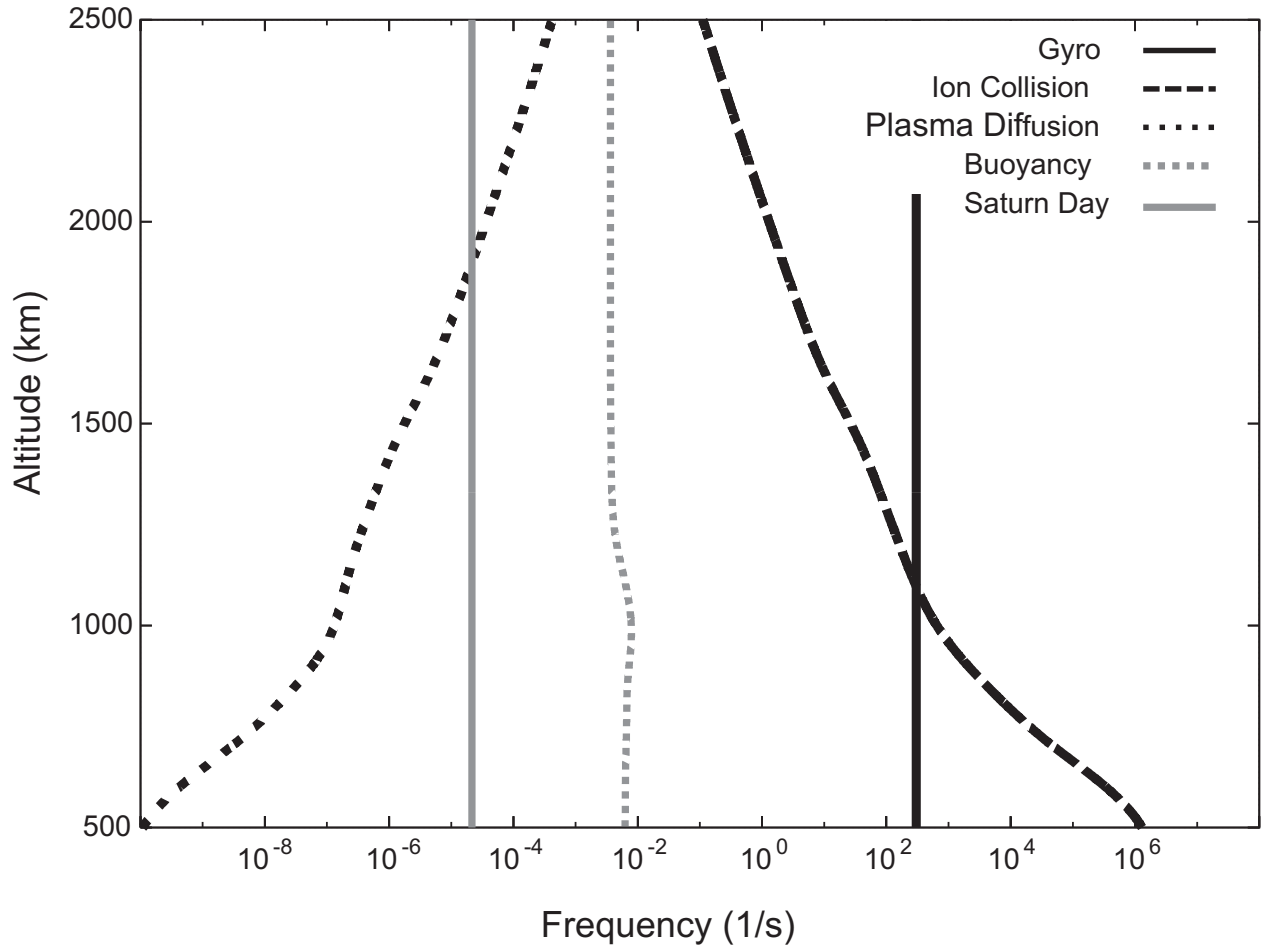


Figure 3: Relevant dynamical time (frequency) constants:  $H^+$  gyro frequency (black solid line);  $H^+$  collisional frequency (black dashed line);  $1/t_d$ , where  $t_d$  is the  $H^+$  diffusion time constant (black dotted line); buoyancy frequency of the atmosphere (gray dotted line);  $1/t_S$ , where  $t_S$  is the length of one Saturn day (gray solid line).

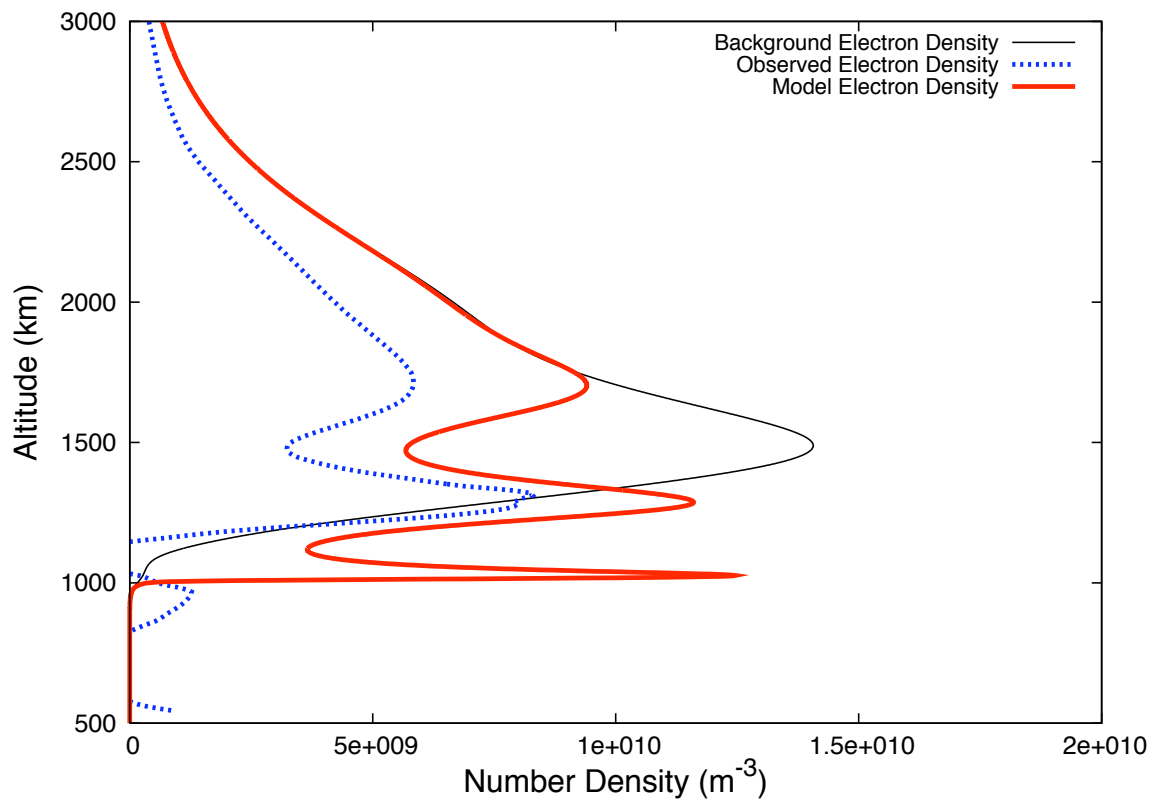


Figure 4: Large amplitude simulation for the S08 entry occultation. Dotted line - observed electron density; thin black line - initial steady state electron density (no waves); thick solid red line - wave-perturbed electron density after five wave periods.

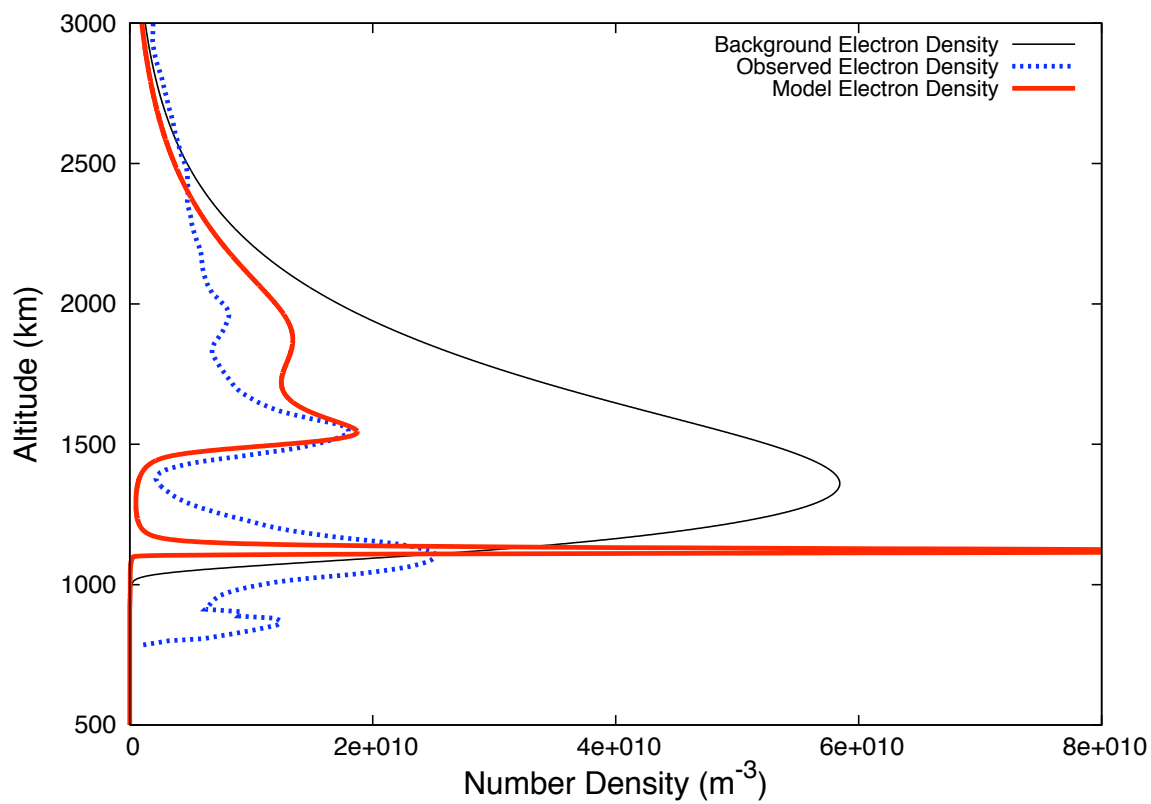


Figure 5: Same as Fig. 4 but for S68 entry.

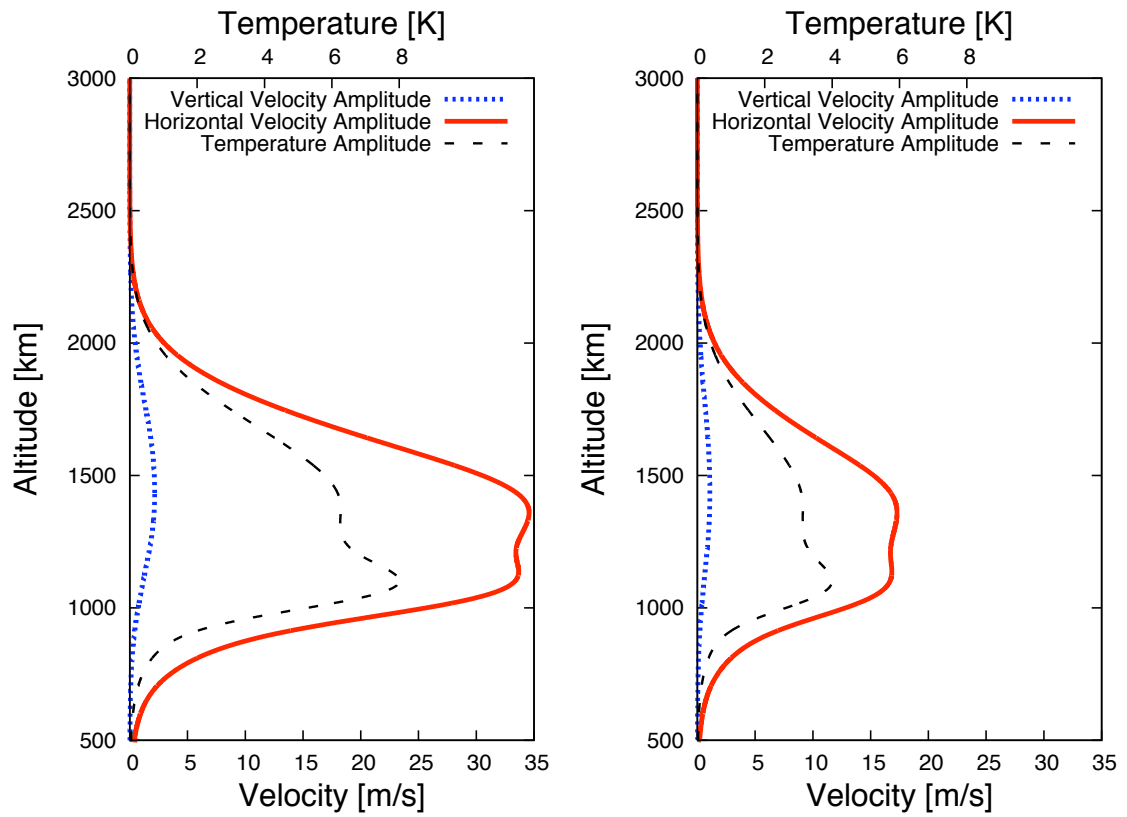


Figure 6: Vertical amplitude profiles of the temperature  $T$ , the horizontal velocity  $V$ , and the vertical velocity  $W$  of the forcing waves in the case of S08 entry occultation (left panel) and the S68 entry occultation (right panel).

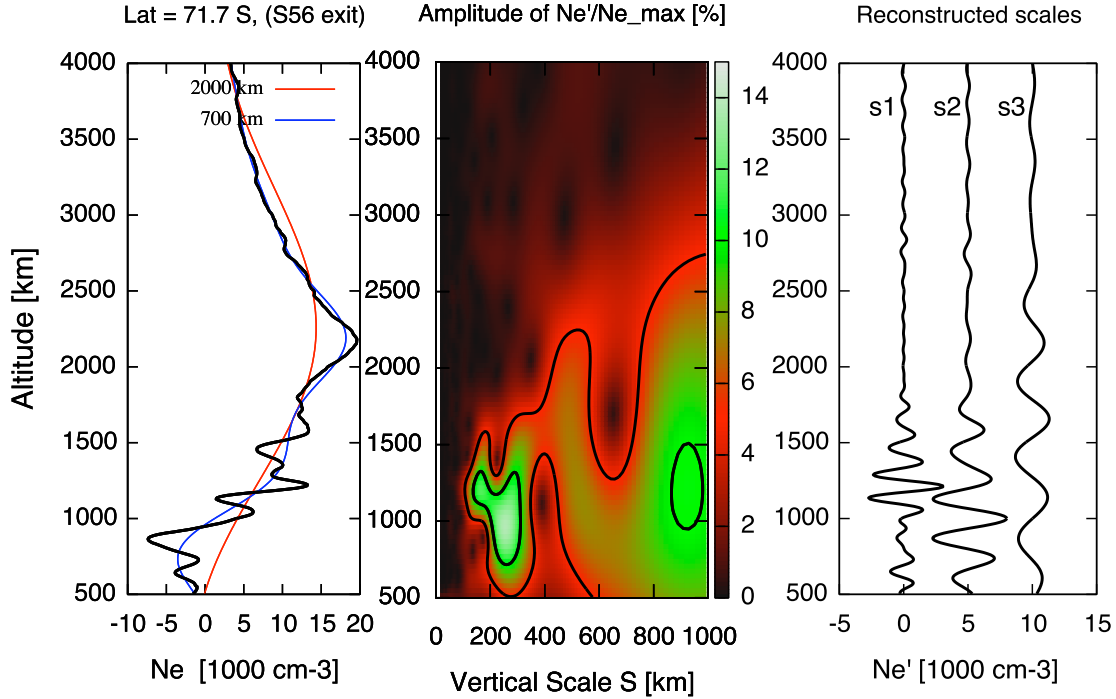


Figure 7: S56 exit radio occultation. Left panel: observed electron density profile (black line); wavelet reconstruction for scales longer than 700 km (blue line); wavelet reconstruction for scales longer than 2000 km (red line). Central panel: Wavelet decomposition map for the S56 exit observation. The amplitude of the vertical variations in the observed  $N_e$  profile is shown as a function of scale and altitude. Contours (solid black lines) are drawn at 5% increments. Right panel: Reconstruction of the detected scales  $s_1 = 165$  km,  $s_2 = 250$  km,  $s_3 = 500$  km. The reconstructed scales are shifted on the horizontal axis for clarity.

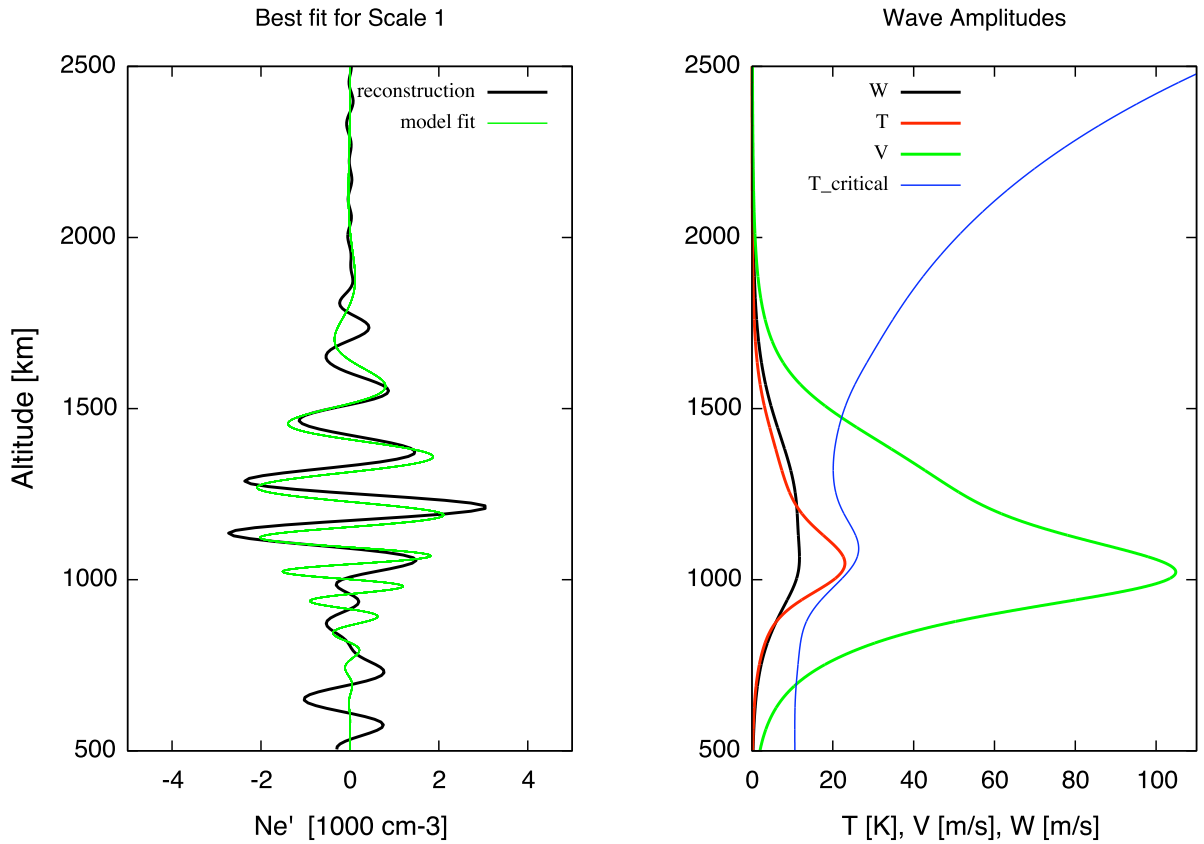


Figure 8: Best fit for scale 1. Left panel: Wavelet reconstruction for scale 1 ( $s_1 = 165$  km) (black line) and the best fit to the data (green line) based on our analytical small-amplitude model of a gravity wave interaction with the ionosphere. Right panel: Vertical amplitude profiles of the temperature  $T$ , horizontal velocity  $V$ , and vertical velocity  $W$  of the forcing wave. The critical temperature  $T_{cr}$  is shown as a blue line. Note that this wave is close to breaking conditions.

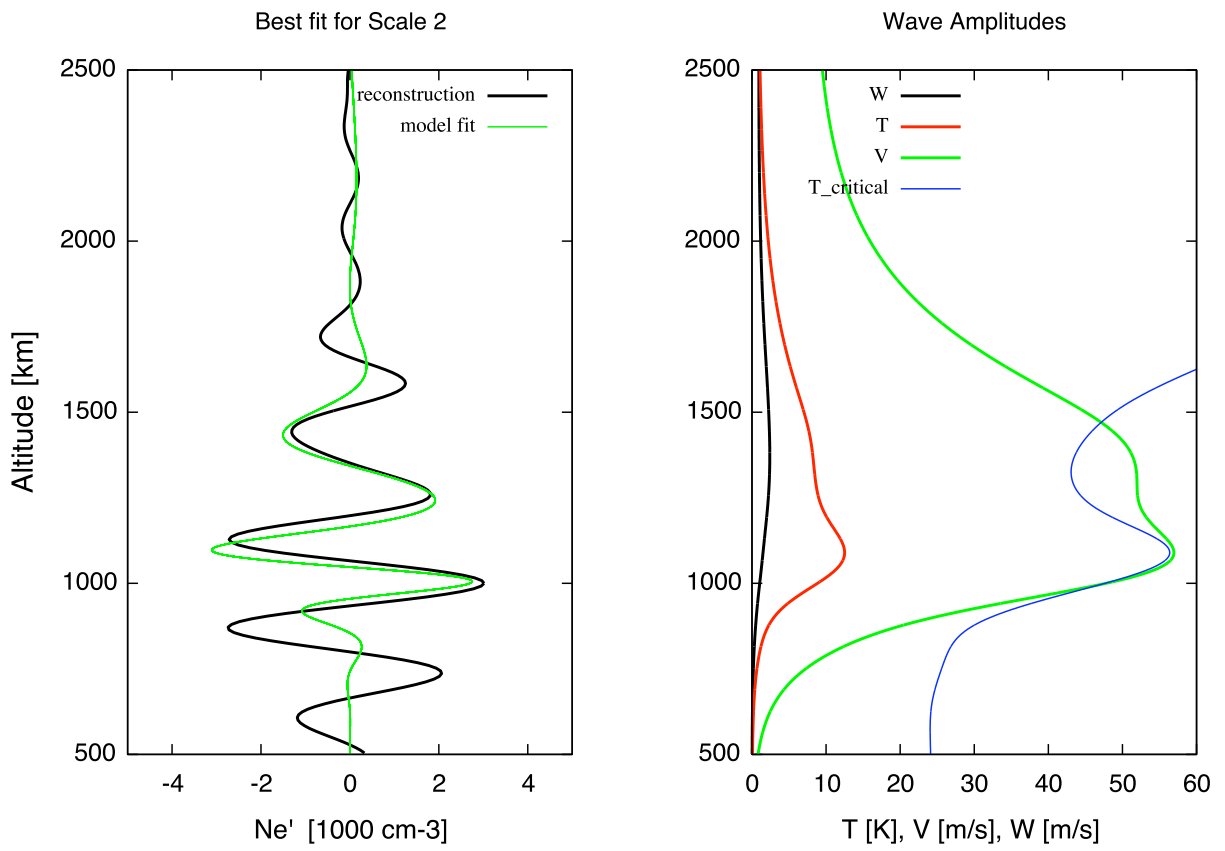


Figure 9: Same as in Fig. 8 but for scale 2 ( $s_2 = 250 \text{ km}$ )

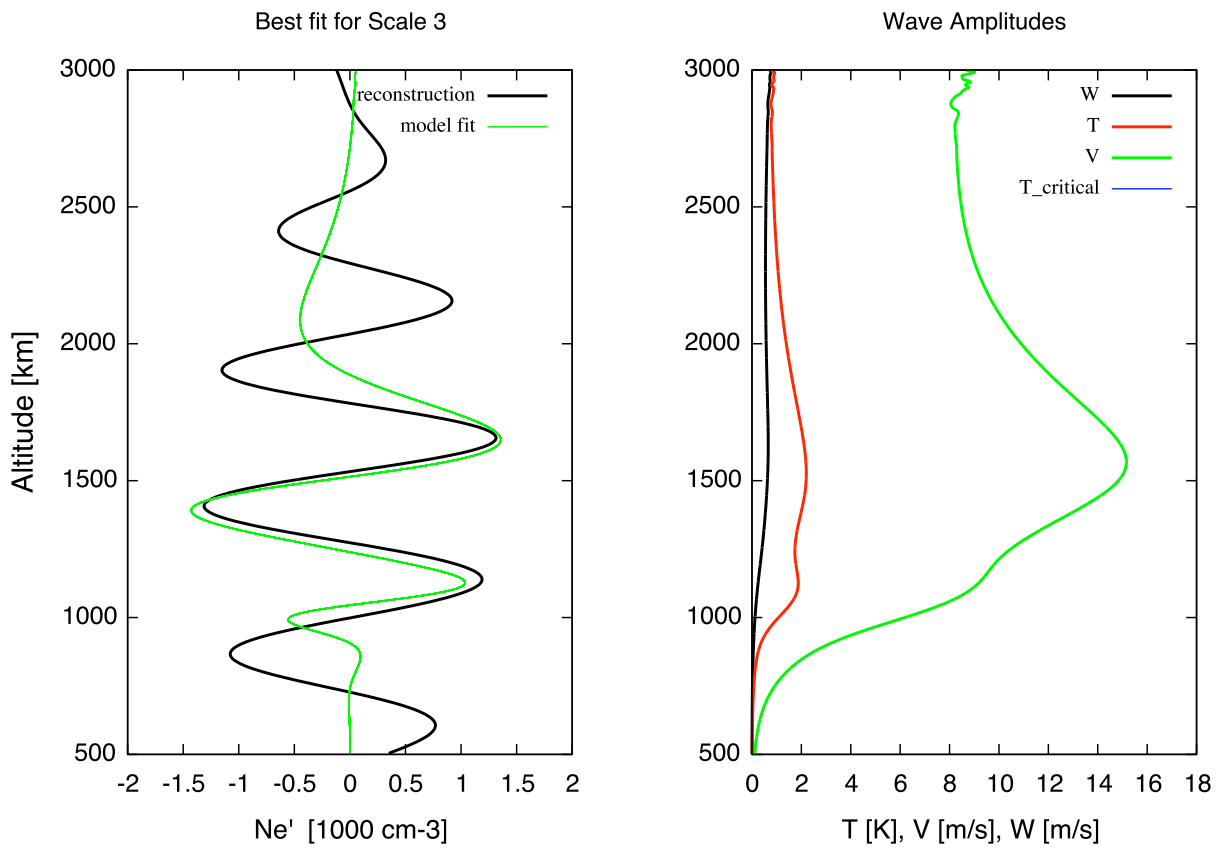


Figure 10: Same as in Fig. 8 but for scale 3 ( $s_3 = 500$  km).

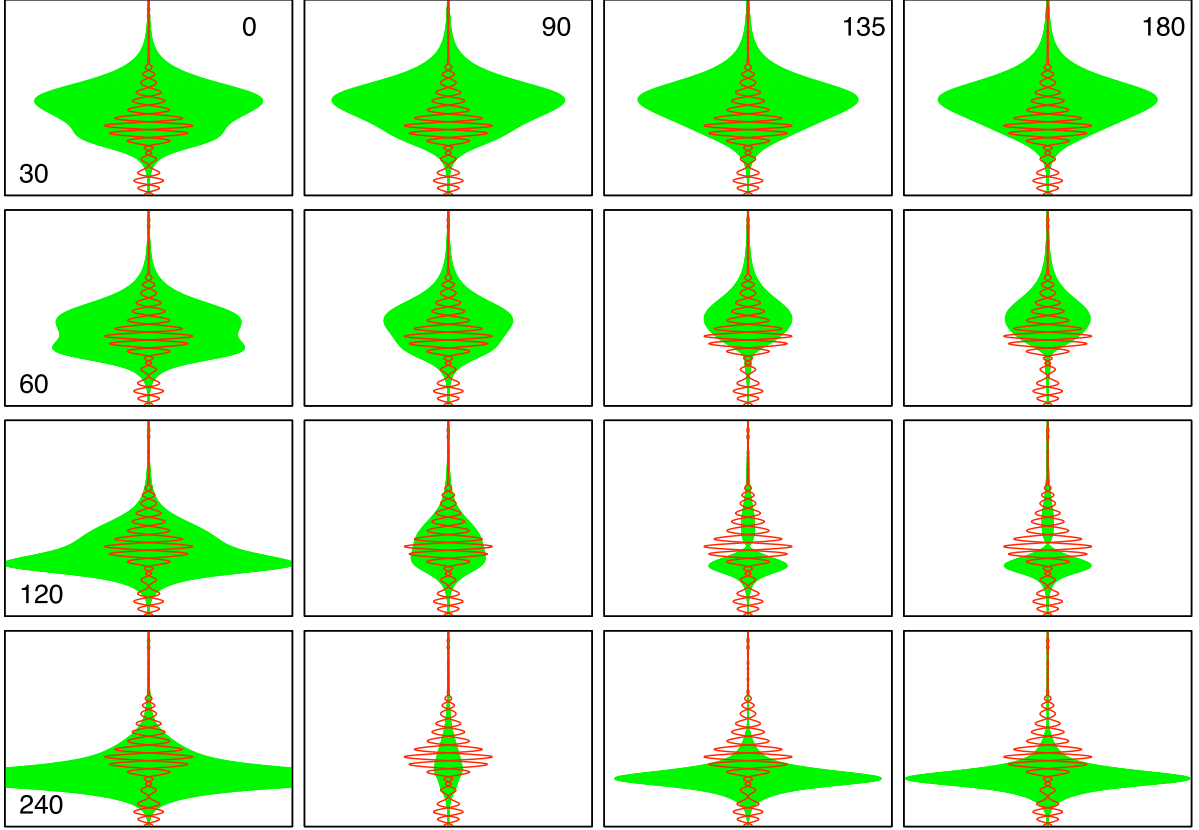


Figure 11: Response table for scale 1. The modeling is done for a wave with  $\lambda_z(z_{max}) = 165$  km ( $\lambda_z(z^*) = 93$  km). The period of the wave is shown in the bottom left corner and the angle of propagation  $\alpha$  is given in the top right corner of the most left and top panels. Panels in the same row show a wave with the same period and panels in a given column have the same angle  $\alpha$ . Each panel shows the amplitude of the resulting electron density perturbations (the contour of the green shaded area) and the s1 scale (red line), plotted once with a positive and once with a negative sign). From the shown cases the closest fit is achieved for  $\tau = 120$  min and  $\alpha = 90^\circ$ . Our best fit is for  $\tau = 120$  min and  $\alpha = 108^\circ$ (not shown here).

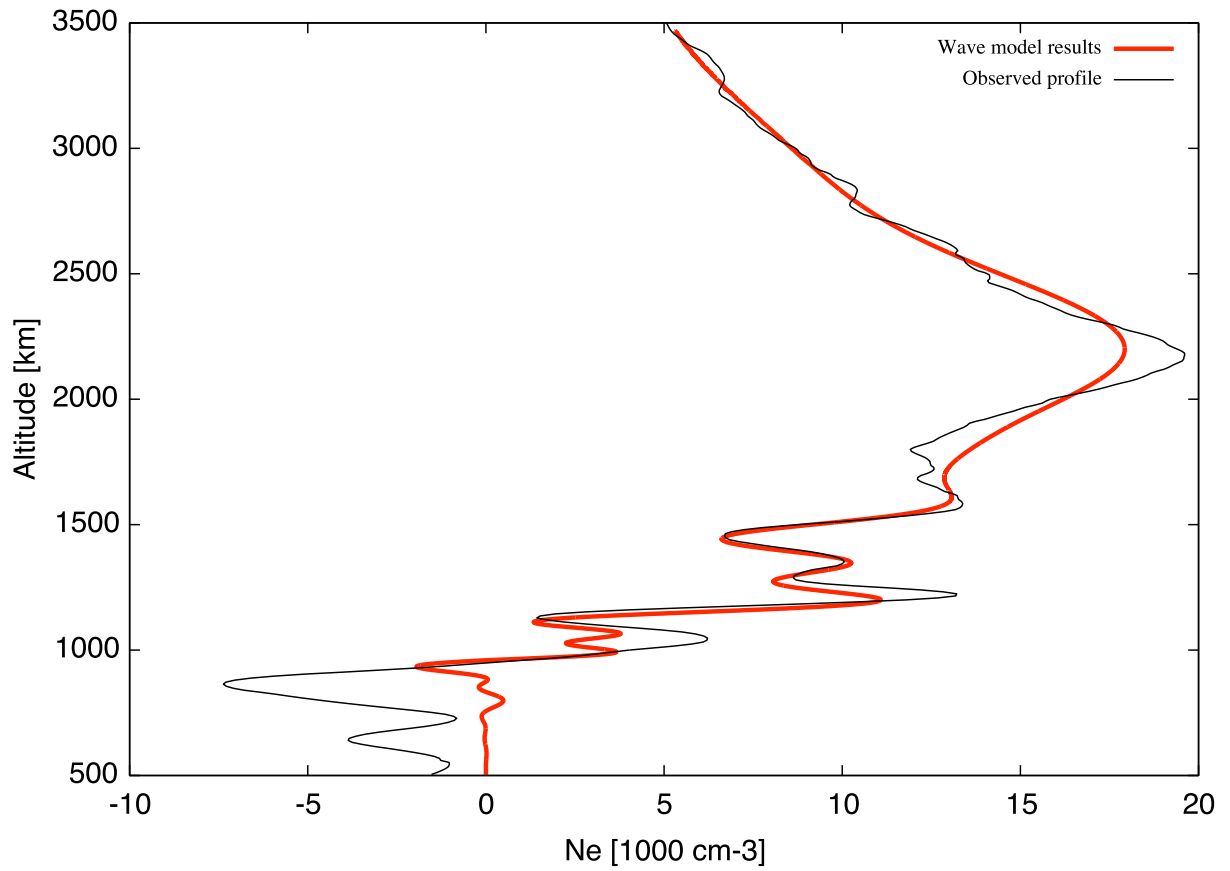


Figure 12: Comparison between S56 exit observation (black line) and the small-amplitude simulation model (red line). The ionospheric results from the three waves are added together and superimposed on the background electron density profile shown in Fig. 7.